INL/JOU-22-65561-Revision-0



# Tensile behavior of diffusion bonded AA6061 - AA6061 with variation in cooling method

August 2023

Dennis D Keiser Jr, Abhishek Mehta, Jeongmin Woo, Jeffrey J Giglio, Jan-Fong Jue, James I Cole, Yongho Sohn

Changing the World's Energy Future

INL/JOU-22-65561-Revision-0

# Tensile behavior of diffusion bonded AA6061 - AA6061 with variation in cooling method

**Dennis D Keiser Jr, Abhishek Mehta, Jeongmin Woo, Jeffrey J Giglio, Jan-Fong Jue, James I Cole, Yongho Sohn**

**August 2023**

**Idaho National Laboratory**
**Idaho Falls, Idaho 83415**

**http://www.inl.gov**

**Prepared for the**
**U.S. Department of Energy**
**Under DOE Idaho Operations Office**
**Contract DE-AC07-05ID14517**

# Tensile behavior of diffusion bonded AA6061 - AA6061 with variation in cooling method

Abhishek Mehta, Jeongmin Woo, Jeffrey J. Giglio, Jan-Fong Jue, Dennis D. Keiser Jr., James I. Cole, Yongho Sohn

**Abstract**

Hot isostatically pressed AA6061 cladding is an important structural component of the high performance, Zr-laminated U-10Mo monolithic fuel system for the application in research and test reactors. In this study, the mechanical behavior of two diffusion bonded aluminum alloy, AA6061, was examined using tensile testing. Solid-to-solid diffusion bonding between two pieces of AA6061 was performed by isothermal annealing at 560 °C for 1.5 h, and diffusion couples were subsequently cooled via three different cooling methods: furnace cooling, air cooling, and water quenching. Dog-bone shaped tensile specimens, with 10 mm in gauge length (with diffusion bonded interface in the middle), and 1.5 × 1.5 $mm^2$ gauge cross-sections, were fabricated from the diffusion bonded AA6061 by electro-discharge machining. Yield strength (% EL at failure) of furnace cooled, air cooled and water quenched tensile specimens determined was 82–89 MPa (10–30%), 112–116 MPa (10–14%), and 149–164 MPa (10–17%), respectively. This variation in mechanical behavior was examined with cooling-rate dependent, concentrated precipitation of $Mg_2Si$ at the diffusion bonded interface, with due respect for mechanical properties of the AA6061 alloy that inherently vary as a function of cooling rate from 560 °C. Finite element analysis using ABAQUS was employed to augment experimental findings with the appropriate microstructural constituents and alloy properties. Results suggest that the strength is dominated by matrix/bulk properties of AA6061, while ductility is strongly influenced by the cooling method dependent presence of $Mg_2Si$ precipitates at the interface.

**Keywords**

Diffusion bonding

AA6061

Microstructure

Mechanical testing

Finite element analysis

## 1. Introduction

The United States High Performance Research Reactor (USHPRR) conversion program aims to support non-proliferation efforts by replacing high enriched uranium (HEU, U235 > 20 at. %) with low enriched uranium (LEU, U235 < 20 at. %) fuels [[1], [2], [3]]. The program proposes the use of U-Mo fuel alloy in monolithic plate design, which has a minimum required effective uranium density of 14 $g/cm^3$. The monolithic design involves encapsulating Zr-laminated U-10Mo fuel

within two cladding pieces made of aluminum alloy 6061 (AA6061) through hot isostatic pressing (HIP) at 560°C for 1.5 h [[4], [5], [6], [7], [8], [9]]. The AA6061 cladding possesses desirable properties such as strength, high thermal conductivity, and low neutron absorption cross-section. However, it is also exposed to extreme in-reactor conditions, including stress, temperature, neutron fluence, and their gradients, as it is the outermost layer of the monolithic fuel plate. So, the mechanical integrity of the interface between the two AA6061 claddings is crucial for the structural integrity and proper performance of the monolithic fuel system. Recent research by Jue et al. [10] has shown that the HIP-bonded interface between the two AA6061 cladding pieces in monolithic fuels may delaminate or crack during reactor operation, compromising the overall mechanical integrity.

This study aims to systematically examine the mechanical behavior, *in tension,* of the diffusion bonded AA6061 alloys using quasi-static tensile testing. Diffusion bonding between the two AA6061 alloys was carried out by isothermally annealing three solid-to-solid diffusion couples at 560 °C for 1.5 h. After the high temperature diffusion bonding anneal, the diffusion couples were cooled using three different methods, namely water quenching, air cooling, and furnace cooling. Subsequently, the diffusion couples were wire electro-discharge machined (EDM) into tensile bars and subjected to tensile testing. To supplement the experimental results, finite element analysis (FEA) was carried out to better understand the impact of post-anneal cooling rates on the tensile properties of diffusion bonded AA6061. The FEA examined the effects of concentrated precipitation of $Mg_2Si$ at the interface bond-line and matrix/bulk properties associated with post-anneal cooling methods to better understand the mechanical behavior of diffusion bonded AA6061.

## 2. Experimental details

### 2.1. Fabrication of diffusion couples

The nominal composition of AA6061 used to fabricate the diffusion couple is reported in Table 1. T6 heat-treated AA6061 was cut into cubes using a low-speed diamond saw, with an approximate dimension of 10 mm × 10 mm × 10 mm. One face of the cube was polished down to 1 μm, while maintaining a minimum cube dimension of 10 mm × 10 mm × 8.5 mm. All surfaces were then cleaned ultrasonically in an ethanol bath and dried using forced air. The metallographically prepared surfaces of the two AA6061 pieces were then placed in contact by using two stainless steel clamping jigs. Thin alumina spacers were placed between the alloy and the stainless-steel jig to prevent any elevated temperature interaction between AA6061 and the stainless-steel jig. The assembled diffusion couple, as shown in Fig. 1(a), along with a tantalum foil (i.e., oxygen getter), was placed in a quartz tube, evacuated to a pressure of $8.0 \times 10^{-6}$ torr or better, and alternately flushed with high purity Ar and $H_2$ gas. The evacuation and flushing process were repeated several times, and the quartz tube was finally backfilled with high purity Ar at 272 torr to create approximately one atmospheric pressure at 560 °C. To complete the diffusion couple preparation, the quartz tube was sealed using an oxy-acetylene torch. Further information on the diffusion couple fabrication process can be found in our previous work [[11], [12], [13], [14], [15], [16], [17], [18]].

Table 1. Nominal composition of AA6061 used for the diffusion couple fabrication.

| Elements | Al | Mg | Si | Ti | Cr | Mn | Fe | Ni | Cu | Zn |
|---|---|---|---|---|---|---|---|---|---|---|
| Composition (wt.%) | Bal. | 1.14 | 0.78 | 0.11 | 0.24 | 0.09 | 0.28 | 0.10 | 0.21 | 0.06 |

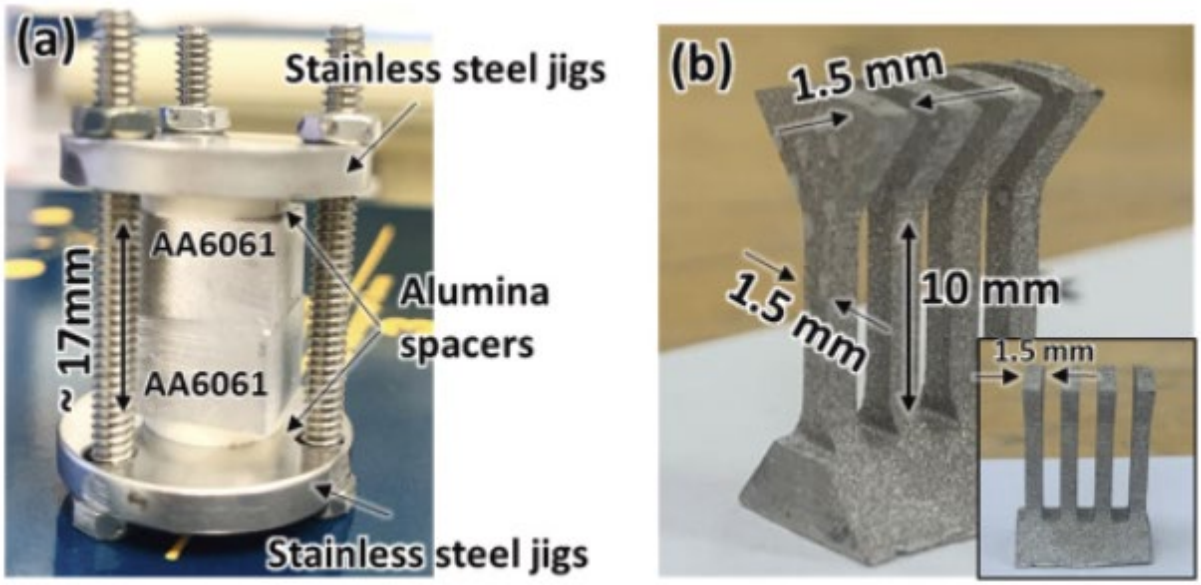


Fig. 1. (a) Assembled diffusion couple in stainless steel jigs. (b) Tensile rack with four tensile bars with 10 mm gauge length and 1.5 mm × 1.5 mm cross-section obtained after wire electro-discharge machining of the diffusion couple.

Three diffusion couples were annealed isothermally for 1.5 h in a Lindberg/BlueTM three-zone tube furnace which was pre-stabilized at 560 °C. To ensure the accuracy of the temperature, an external Type-K thermocouple was used to monitor the temperature, and the measured temperature was within ±2 °C of the setpoint temperature. After annealing, the diffusion couples were cooled using three different methods: water quenching, air cooling, and furnace cooling. The estimated cooling rates for each method are shown in Fig. 2. These cooling curves were determined by Newtonian cooling, described by Ref. [19]:

$$\frac{dT}{dt} = \frac{\alpha A}{C}(T_S - T) = k\ (T_S - T) \tag{1}$$

where α is the heat transfer coefficient, A is the surface area of the specimen, C is the heat capacity of the body, TS is the ambient temperature (25◦C), k is the cooling rate parameter (αA C). Solution of the cooling rate given by Eq. (1) is expressed as:

$$T(t) = T_s + (T_o - T_s)\, e^{-kt} \tag{2}$$

where $T_o$ is the initial temperature (560°C). Therefore, the cooling rate parameter, $k$ ranged from $2.7 \times 10^{-3}$ $s^{-1}$ to $1.0 \times 10^{-4}$ $s^{-1}$, respectively, for air cooling and furnace cooling.

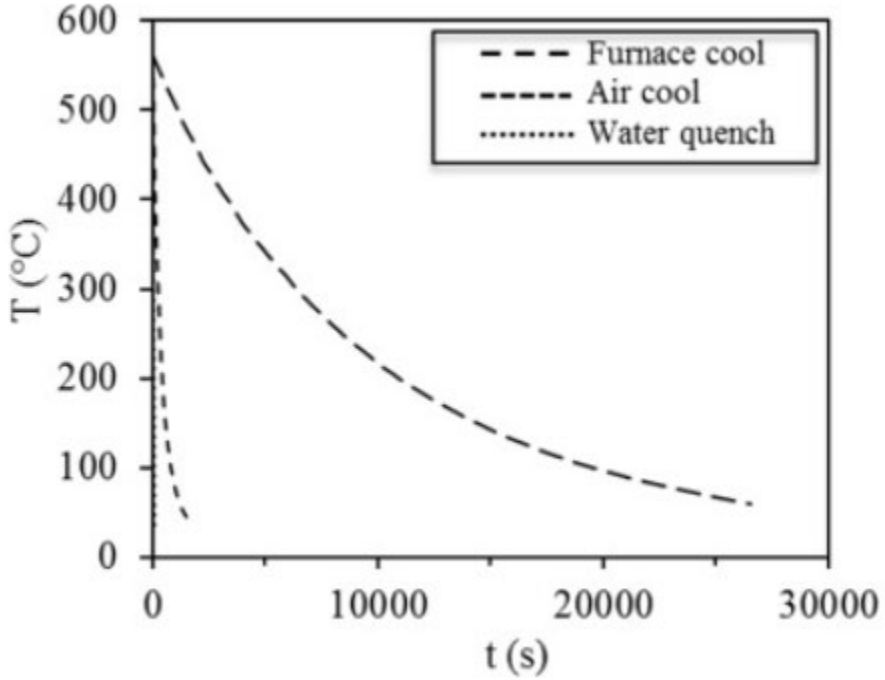


Fig. 2. Cooling curves after furnace cooling, air cooling and water quenching.

### 2.2. Tensile testing and microstructural characterization

To prepare the diffusion annealed samples for tensile testing, quick-setting glue was applied to the surfaces to minimize damage during wire EDM. Four tensile specimens were prepared from each of the water quenched (WQ), air-cooled (AC), and furnace cooled (FC) diffusion couples. The tensile specimens had a 10 mm gauge length and 1.5 mm × 1.5 mm cross-section, as per the ISO/ASTM AWI 52909 standard for miniature tensile testing without significant concern for scale/surface effect. The specimens were identified using alpha-numeric identifiers, e.g., WQ/AC/FC 1 through 4. However, one tensile bar from the edge of the water quenched diffusion couple (WQ4), and two tensile bars from each edge of the air-cooled diffusion couple (AC1 and AC4) disbanded during wire EDM. Thus, only the two middle tensile specimens of each tensile rack were considered to avoid any edge-damage effect from diffusion couple bonding/cooling and/or wire EDM, and mechanical properties were assessed from these two specimens. Fig. 1(b) shows the dimensions of the tensile specimens.

The tensile specimens were tested under quasi-static conditions [20] at room temperature using a full-field, 2-D strain measurement technique called digital image correlation (DIC) system provided by Correlated Solutions, Inc. The surfaces of the specimens were painted before testing to ensure accurate strain measurement. The DIC system provided strain measurements normal to the uniaxial loading direction, and the quasi-static strain rate was maintained at $5 \times 10^{-4}$ $s^{-1}$. Microstructural features of the diffusion couple interfaces and fractured surfaces from tensile

testing were observed using Zeiss™ Ultra-55 field emission electron microscope (FE-SEM) equipped with X-ray energy dispersion spectroscopy (XEDS).

### 2.3. Simulation of the tensile testing using finite element analysis

The post-anneal cooling rate influences both the linear density of $Mg_2Si$ precipitates [21] at the diffusion-bonded interface and the matrix/bulk properties of AA6061 [22,23]. It can be challenging to experimentally distinguish the effect of each factor on the tensile behavior of the diffusion-bonded AA6061. Therefore, finite element analysis (FEA) was employed to simulate the tensile loading of diffusion-bonded AA6061 by independently varying the linear density of $Mg_2Si$ and the matrix/bulk properties of AA6061.

To simulate the effect of $Mg_2Si$ precipitates on the tensile behavior of diffusion bonded AA6061, only a portion of the tensile bar was modeled, since the precipitates are much smaller than the specimen size. The $Mg_2Si$ precipitates were assumed to have an oblate geometry with an aspect ratio of 1:5 and were distributed only at the interface, as shown in Fig. 3. To examine the effect of the precipitate linear density, half of the precipitates were located at each end of the tensile bar, and the spacing between them was varied to change the number of precipitates, as shown in Table 2. The longitudinal direction of the tensile bar was parallel to the Z-axis, and nodes on the X–Y plane were clamped, while nodes on the other side were moved in the Z-direction to simulate tensile loading.

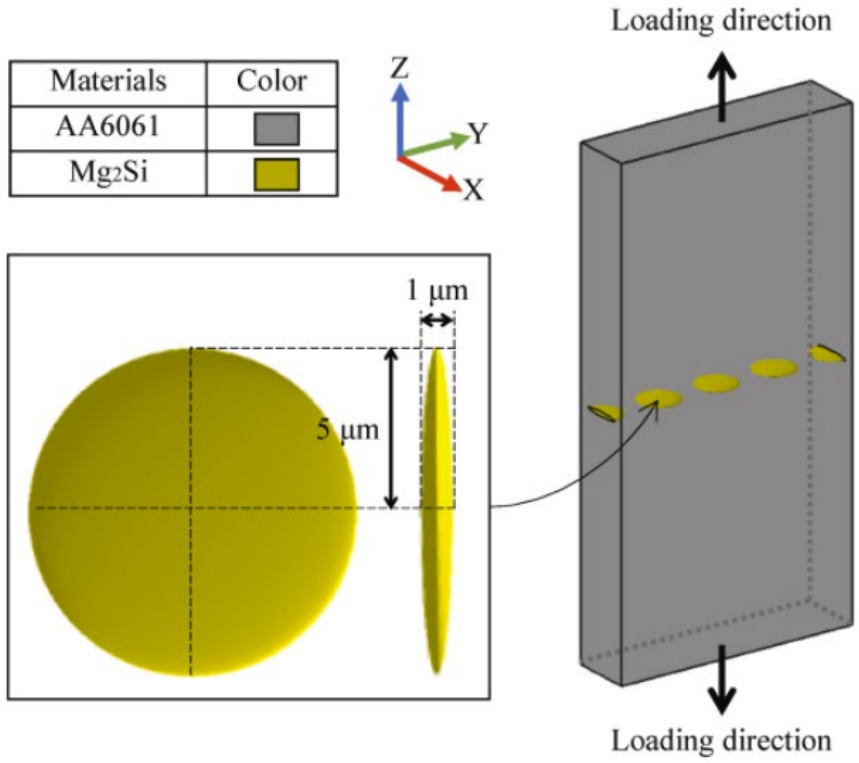


Fig. 3. A schematic illustration of the finite element model for tensile testing.

Table 2. Linear density examined for the precipitates and corresponding spacing between precipitates in FEA using ABAQUS.

| Assumed precipitate linear density (%) | Spacing between precipitates ($\mu m$) |
|---|---|
| 50.0 | 10 |
| 33.3 | 20 |
| 0.0 | Infinite |

The mechanical properties of AA6061 are dependent on the heat treatment, i.e., O, T4, or T6. As the cooling rate increases, strength increases and ductility decreases. To represent the material properties of AA6061 specimen for each cooling method, different material properties of AA6061 were adopted. The material properties utilized in the FEA are listed in Table 3, and are based on prior studies [[24], [25], [26], [27], [28]]. Unfortunately, information on the ultimate tensile strength (UTS) of the $Mg_2Si$ precipitate phase was not readily available in the literature [26,29]. Therefore, the UTS of the $Mg_2Si$ was estimated by assuming that the ratio of UTS to Vickers hardness has a similar value, based on other silicides that have been examined more extensively for mechanical properties. As noted in Table 3, other estimations were for the mechanical properties of $Mg_2Si$. It should be noted that this estimation *did not affect* the relative variations in simulation results from the three cooling rates; however, it did alter the absolute magnitude of the results.

Table 3. Material properties adopted for the finite element analysis using ABAQUS.

| Properties | AA6061-O (Used to represent FC) | AA6061-T4 (Used to represent AC) | AA6061-T6 (Used to represent WQ) | $Mg_2Si$ |
|---|---|---|---|---|
| E (GPa) (Modulus of elasticity) | 68.9 | 68.9 | 68.9 | 110.03 [26,29] |
| Y.S., $\sigma_Y$ (MPa) | 55.2 | 145 | 276 | – |
| UTS, $\sigma_{UTS}$ (MPa) | 125 | 241 | 310 | 91.6 (Estimated) |
| El at failure (%) | 25 | 22 | 12 | 0.093 (Estimated) |
| Poisson's Ratio | 0.33 [27] | 0.33 [27] | 0.33 [27] | 0.17 [26] |
| Density ($kg/m^3$) | 2702 [27] | 2702 [27] | 2702 [27] | 1990 [26] |
| Equivalent plastic strain in uniaxial tension | 1.26 [24] | 0.98 (Assumed) | 0.7 [25] | 0.0001 (Estimated) |
| Mean value of the stress triaxiality in uniaxial tension | 0.39 [24] | 0.3612 (Assumed) | 0.3324 [25] | 2.5 (Estimated [22]) |

To model the fracture, stress triaxiality dependent fracture initiation criterion was applied. Stress triaxiality, η is a ratio of the hydrostatic stress to the Von Mises stress, and can be expressed as [28]:

$$\eta = \frac{\frac{\sigma_{xx}+\sigma_{yy}+\sigma_{zz}}{3}}{\sqrt{\frac{(\sigma_{xx}-\sigma_{yy})^2+(\sigma_{yy}-\sigma_{zz})^2+(\sigma_{zz}-\sigma_{xx})^2+6\left(\sigma_{xy}{}^2+\sigma_{yz}{}^2+\sigma_{zx}{}^2\right)^2}{2}}} \quad (3)$$

where $\sigma_{ij}$ denotes the components of the stress tensor. The equivalent plastic strain to fracture $\bar{\varepsilon}_D^{pl}$ can be expressed as a function of stress triaxiality η. The relationship between the equivalent plastic strain to fracture $\bar{\varepsilon}_D^{pl}$ and the stress triaxiality η is obtained by conducting a series of upsetting tests, shear tests, and tensile tests as described by Wierzbicki and co-workers [30,31]. The fracture initiation criterion assumes that a damage is initiated when the following condition is satisfied [32]:

$$\omega_D = \int_0^{\bar{\varepsilon}_D^{pl}} \frac{1}{\bar{\varepsilon}_D^{pl}(\eta)} d\bar{\varepsilon}^{pl} = 1 \quad (4)$$

where $\bar{\varepsilon}^{pl}$ denotes the equivalent plastic strain, and ωD is a state variable that increases monotonically with plastic deformation. Since FEA models are simulating the tensile tests, equivalent plastic strain and stress triaxiality under a uniaxial tensile loading condition were utilized for FEA to model the fracture behavior. The equivalent plastic strain and stress triaxiality of AA6061-O and AA6061-T6 were obtained from Refs. [24,25] respectively. The equivalent plastic strain and stress triaxiality of AA6061-T4 were assumed to be the average of AA6061-O and T6. The Mg2Si phase is a brittle intermetallic phase in comparison to the ductile α-Al matrix of AA6061. Therefore, the stress triaxiality of Mg2Si was assumed to be 2.5, given that typical brittle phases have a stress triaxiality between 2 and 3 [28] and fail by brittle cleavage fracture mode. The equivalent plastic strain of Mg2Si was assumed to be 0.0001, as reported in Table 3.

For AA6061-O, work-hardening was corrected using linear piecewise hardening, which was determined to be a more accurate approach [24]. On the other hand, the stress-strain behaviors of AA6061-T4 and -T6 were expressed and extrapolated using Hollomon's equation and the corresponding strain-hardening exponent and strength coefficient [33, 34]. The simulations were performed using the ABAQUS 6.10 software suite, employing the explicit code, ABAQUS/EXPLICIT. To reduce computation time, 8-node hexahedron elements with reduced integration C3D8R were used. The simulations were carried out on a computer equipped with 64 GB RAM and an Octa-core processor.

## 3.Microstructural characteristics of diffusion bonded interfaces

Fig. 4 shows backscatter electron micrographs of the diffusion bonded AA6061 specimens after isothermal annealing at 560 ◦C for 1.5 h and cooling by (a) water quenching, (b) air-cooling, and (c) furnace cooling. All specimens exhibited white precipitates containing Al, Fe, and Si, with the stoichiometry of $Al_{19}Fe_4MnSi_2$, which are known to form during casting. However, the extent of

Mg2Si precipitation was different in each specimen. The water quenched specimen did not show any distinct Mg2Si precipitates at the diffusion bonded interface, while air-cooled and furnace-cooled specimens did exhibit Mg2Si precipitates along the bond line. The propensity for Mg2Si precipitation at the interface increased with slower cooling rates.

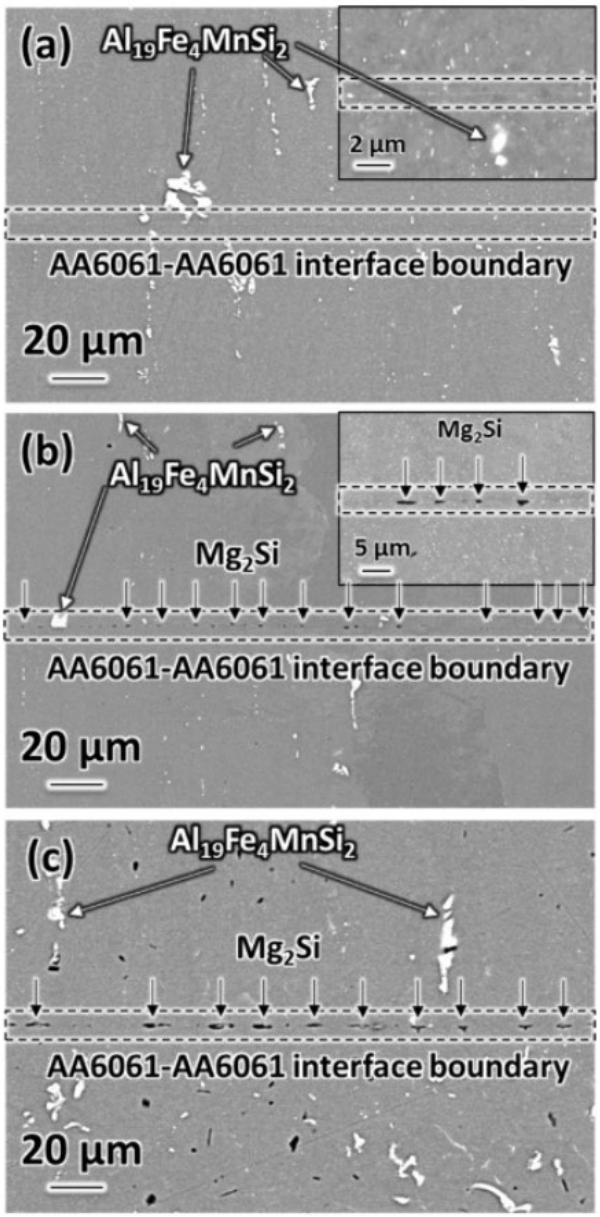


Fig. 4. Representative backscatter electron micrographs from the AA6061 vs. AA6061 diffusion couples isothermally annealed at 560 °C for 90 min, followed by (a) water quenched, (b) air cooled, and (c) furnace cooled.

Isothermal annealing at the HIP temperature of 560 ◦C would not lead to the precipitation of Mg2Si because this temperature is higher than the typical solutionizing temperature for AA6061 (520–540 ◦C), according to the updated solvus line for the solubility of Mg2Si in AA6061 by Amado

and Daroqui [35]. As shown in Fig. 5, the cooling curve for water quenching does not intersect with the TTT (time-- temperature-transformation) curve for Mg2Si formation. However, relatively slow cooling methods can result in Mg2Si formation in AA6061, as presented in Fig. 4. Furthermore, the extent of precipitation is significantly larger in furnace-cooled diffusion couples than in air-cooled diffusion couples. The linear density of Mg2Si precipitates across the diffusion-bonded interface is 0.0%, 17.1%, and 45.8% for water-quenched, air-cooled, and furnace-cooled samples, respectively. The extent of Mg2Si precipitation observed in the AA6061 vs. AA6061 HIP-bonded cladding-cladding interface [10] is similar to that in the furnace-cooled diffusion couple presented in Fig. 4(c). More importantly, these results agree well with the previous experimental observations [18].

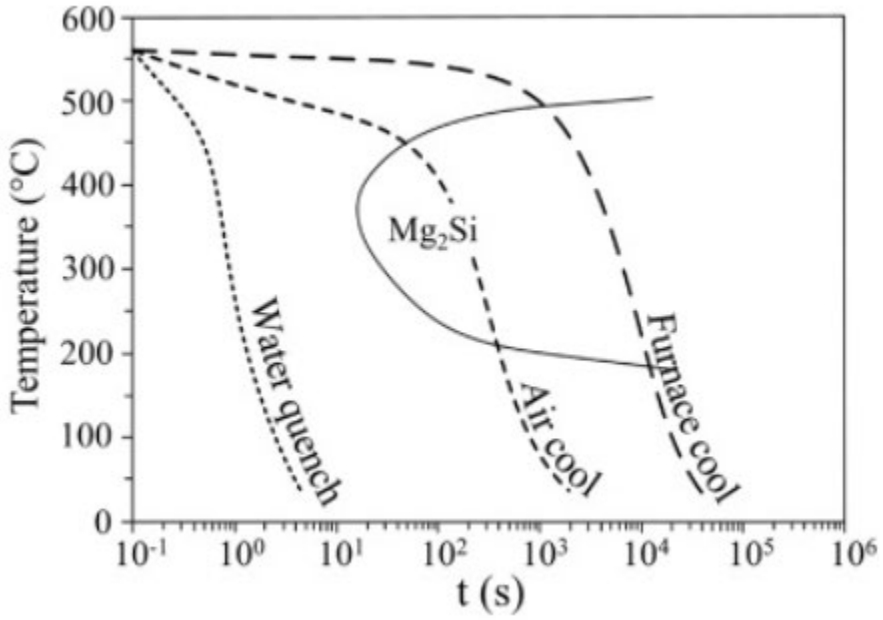


Fig. 5. Cooling rates examined in this study superimposed on the TTT diagram of AA6061 [36].

A mechanism has been postulated to explain the concentrated formation of $Mg_2Si$ at the interface during post-anneal cooling due to the presence of oxygen in the native oxide layer of Al-alloys at the interface [21]. According to this mechanism, the presence of oxygen causes lithophile elements, i.e., Mg and Si, to preferentially diffuse towards the interface. Mg would then preferentially react with oxygen to form nanoscale MgO, leaving remnant Mg to react with Si to form $Mg_2Si$, which becomes concentrated at the interface boundary [21]. This concentrated presence of $Mg_2Si$ precipitates at the interface is believed to affect the mechanical behavior of the HIP bonded AA6061 interface in the monolithic fuel plates.

## 4. Mechanical testing

Fig. 6 displays the engineering stress-strain curves obtained from miniaturized tensile testing of water quenched, air cooled, and furnace cooled specimens, while Table 4 reports the corresponding tensile properties. Aforementioned, tensile samples WQ4, AC1, and AC4 failed during the wire EDM process, as shown in Fig. 6, and were excluded from the analysis to ensure

consistency in avoiding the edge effect of the diffusion couples. Specifically, all tensile samples near the edge of the water quenched tensile rack (i.e., WQ1) and furnace cooled tensile rack (i.e., FC1 and FC4) were excluded. For additional comparison, Table 3 presents the mechanical properties of commercial AA6061 alloy in O, T4, and T6 heat-treated conditions [22].

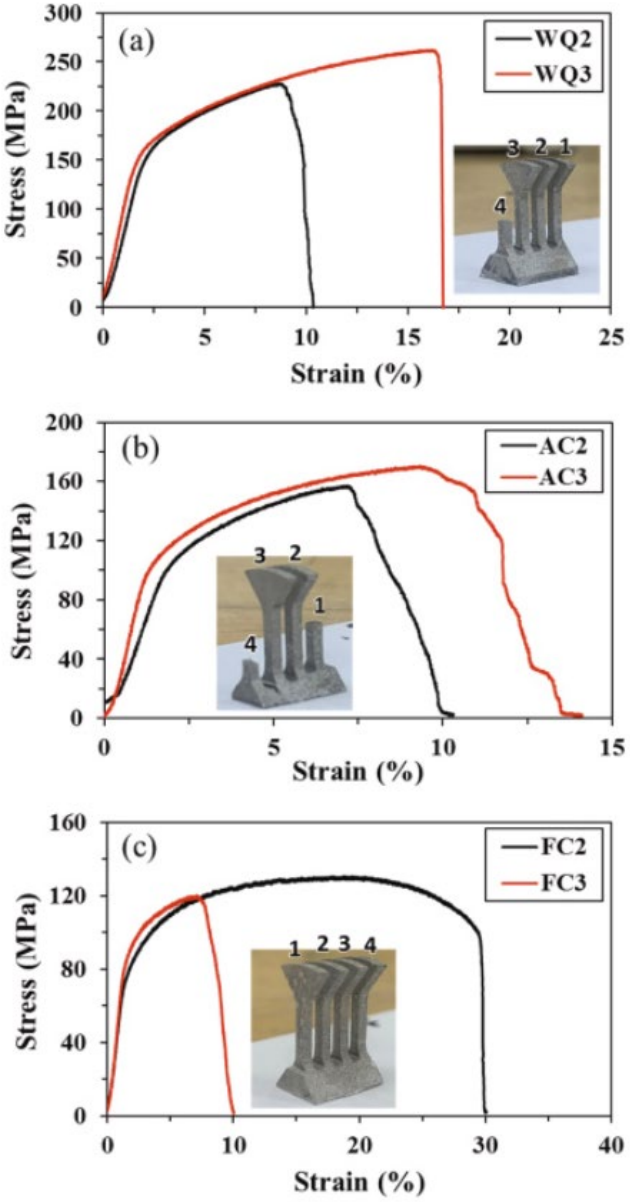


Fig. 6. Engineering stress-strain curves from the diffusion bonded AA6061 tensile specimens fabricated from (a) water quenched; (b) air cooled; and (c) furnace cooled diffusion couples.

Table 4. Mechanical properties determined using miniature tensile testing from diffusion bonded AA6061.

| Diffusion couple | Sample ID | Failure at interface | Yield Strength (MPa) | UTS (MPa) | EL at failure (%) |
|---|---|---|---|---|---|
| Water quenched | WQ2 | Yes | 163.6 | 228.1 | 10.3 |
| | WQ3 | Yes | 149.6 | 262.5 | 16.8 |
| Air cooled | AC2 | Yes | 112.7 | 157.3 | 10.2 |
| | AC3 | No | 116.6 | 170.5 | 14.1 |
| Furnace cooled | FC2 | No | 82.0 | 130.5 | 30.0 |
| | FC3 | Yes | 88.6 | 120.1 | 10.0 |

Water quenched tensile specimens (WQ2 and WQ3) showed the highest strength, with a yield strength of 150–164 MPa, tensile strength of 228–263 MPa, and ductility of 10–17 %. These values are comparable to the yield and tensile strengths of AA6061 after T4 heat treatment and the ductility after T6 heat treatment. Therefore, the water-quenched AA6061/AA6061 diffusion-bonded interface can be characterized as having elastic behavior similar to AA6061-T4 and plastic behavior similar to AA6061-T6 commercial alloys.

Air-cooled specimens, i.e., AC2 and AC3, were stronger than AA6061-O with yield strength of 113–117 MPa, tensile strength of 157–171 MPa, and ductility of 10–14 %. The AC2 sample that fractured at the interface exhibited low ductility of 10%, which was lower than the AC3 sample with partial fracture occurring slightly away from the interface. Furnace cooled diffusion couple samples, i.e., FC2 and FC3, exhibited yield strength (52–60 MPa) and tensile strength (82–89 MPa) similar to AA6061-O (annealed). Tensile specimen which fractured mostly within the bulk AA6061 exhibited ductility of 30 % similar to that of AA6061-O. However, the FC3 sample with a clear fracture at the diffusion bonded interface only elongated 10 % before the failure. So the furnace cooled AA6061/AA6061 diffusion bonded interface can be characterized to have low strength in addition to inconsistency in ductility. This inconsistency in ductility can also be attributed to the inconsistency in the failing interface (due to local microstructural difference), edge defects from the EDM, and local variation diffusivity which affects interfacial bonding characteristics. These deviations are consistent with the other micro- and meso- scale tensile property determination [37].

Microstructure of HIP bonded cladding-cladding interface examined in numerous fuel plates [21] is similar to the furnace cooled diffusion couples containing discontinuous presence of $Mg_2Si$ precipitates, linearly concentrated along the cladding-cladding interfacial bond-line. Slow cooling after HIP would yield a low strength similar to AA6061-O, and inconsistent ductility. The strength and ductility of the water quenched diffusion couples exhibited similar strength and ductility to the T4 and T6 heat treated AA6061 alloys. Air cooled diffusion couples yielded properties in-between these two samples.

In general, strength should increase while ductility should decrease with an increase in cooling rate. In this work, strength followed the anticipated trend, but ductility did not, albeit varying fracture path. Therefore, microstructural features observed in furnace cooled, and to some extent, the air cooled AA6061/AA6061 interface can be attributed to the low strength and low/inconsistent ductility. In other words, this combination of low strength and low ductility (for the sample fractured at the interface) can be attributed to the formation of equilibrium, incoherent β-$Mg_2Si$ precipitates. Excessive precipitation and coarsening of β-$Mg_2Si$ can also lead to depletion of Mg and Si from the α-Al matrix, further reducing of solid solution strengthening in fcc α-Al. This microstructure is not the same as the conventionally T6 heat treated AA6061 (i.e. AA6061 prior HIP), where nano-scale metastable coherent β" precipitates significantly improve the mechanical strength [23]. Higher tensile strength in water quenched tensile specimens may be influenced by the higher residual stresses due to the formation of supersaturated α-Al solid solution. Fig. 7 summarizes experimentally measured properties in tension reported in Table 4 as a function of $Mg_2Si$ linear density at the interface. A clear trend in yield strength, tensile strength, and elongation at fracture as a function of $Mg_2Si$ linear density that varied with cooling method is demonstrated.

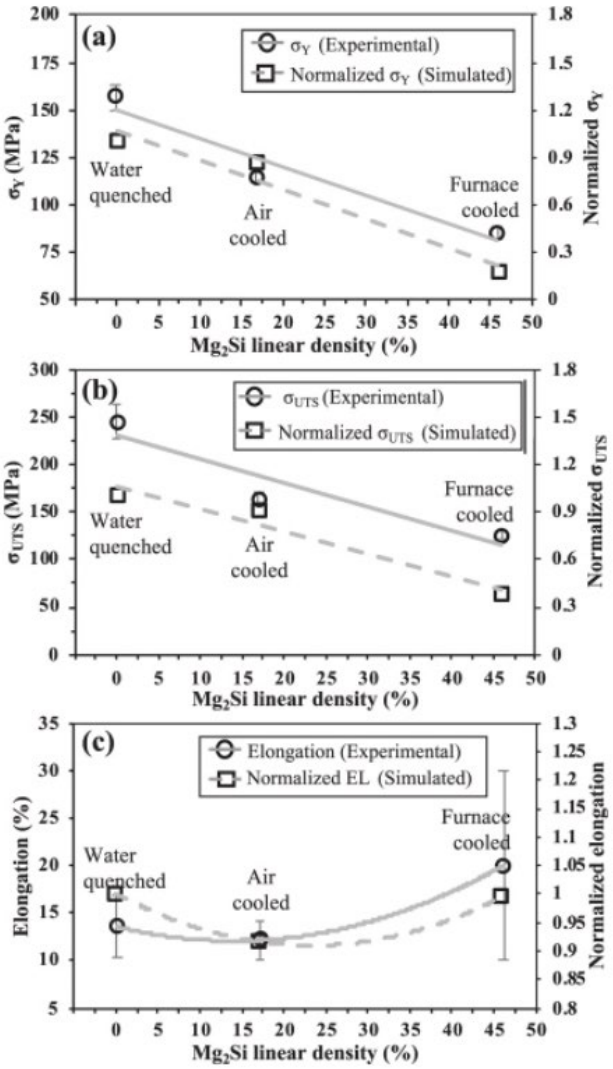

Fig. 7. Variation of absolute and normalized (a) Yield Strength ($\sigma_Y$), (b) Tensile strength ($\sigma_{UTS}$), and (c) Elongation (El) as a function of linear density of $Mg_2Si$ precipitates. Normalized properties are plotted by normalizing to the water quenched samples.

## 5. Characteristics of fracture surfaces

Fig. 8 presents the secondary electron micrographs and corresponding backscatter electron micrographs (inset in secondary electron micrographs) of fracture surfaces. Fig. 8(a) and (b) show the fracture surface from the WQ2 tensile specimen ($\sigma_Y$ = 164 MPa; $\sigma_{UTS}$ = 228 MPa; % EL = 10) that failed at the diffusion bonded interface. Both yield and tensile strengths are higher than AA6061-T4, but the % EL is much lower (i.e., similar to AA6061-T6) for the water quenched diffusion bonded interface. These micrographs show that the fracture occurred completely transgranularly, and so-called "river patterns" with very few micro-voids were observed. The $Al_{19}Fe_4MnSi_2$ precipitates were observed at the bottom of the micro-voids. The $Mg_2Si$ precipitates were not observed on the fractured surfaces, as there were none observed at the interface in WQ samples, as shown in Fig. 4(a). Fracture in the WQ3 specimen ($\sigma_Y$ = 150 MPa; $\sigma_{UTS}$ = 263 MPa; %EL = 16) also occurred at the diffusion bonded interface, and its fracture surfaces are presented in Fig. 8(c) and (d). Similar to the WQ2 sample, the fractured surface of WQ3 sample exhibited few dimples/micro-void, and $Al_{19}Fe_4MnSi_2$ precipitates were observed at the bottom without any presence of $Mg_2Si$ precipitates. Occasional cracking was also observed within $Al_{19}Fe_4MnSi_2$ precipitate as shown in Fig. 8(e) and (f).

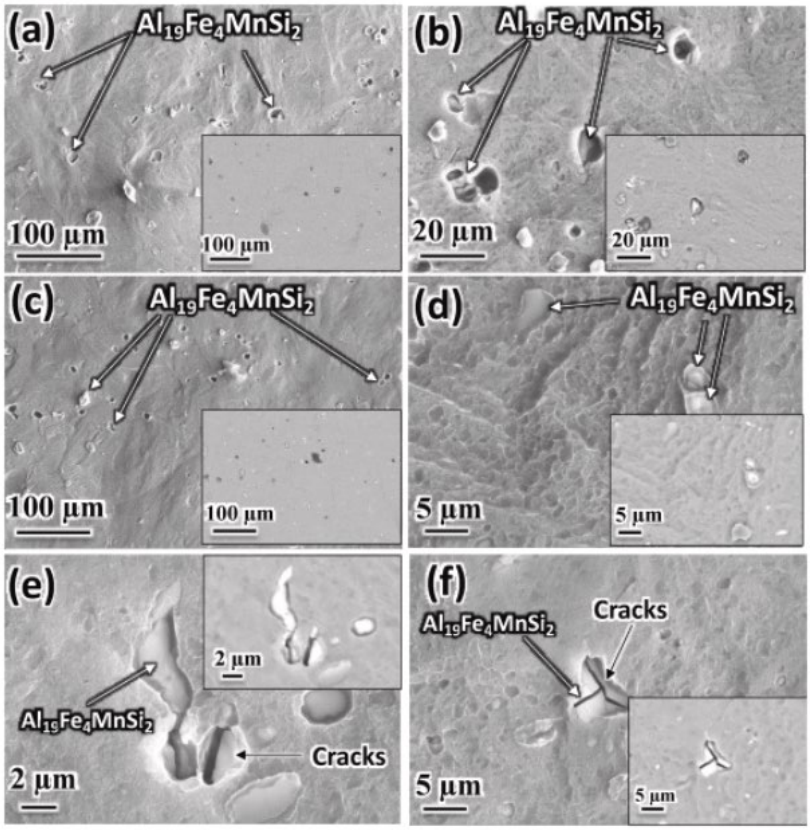

Fig. 8. Secondary electron micrograph and corresponding back scatter electron micrograph (inset) from the fracture surface of the (a,b) WQ2 and (c,d) WQ3 tensile specimens. (e,f) high magnification micrographs identified cracking within $Al_{19}Fe_4MnSi_2$ precipitates at the bottom of the micro-voids.

Fig. 9 presents the secondary electron micrographs from the fracture surface of the air cooled tensile specimen. Fracture in the AC2 occurred near the diffusion bonded interface ($\sigma_Y$ = 113 MPa; $\sigma_{UTS}$ = 157 MPa; % EL = 10). The strengths are higher than AA6061-O, but lower than AA6061-T4. Fig. 9(a) and (b) present the fracture surfaces from the AC2 specimen, which consisted of a few large cleavage planes. Cracks were also observed in AC2, which possibly initiated from the edge of the fractured surface. The fracture surfaces also had the cracking within the $Al_{19}Fe_4MnSi_2$ precipitates. Fracture path in the AC3 sample followed within the bulk AA6061 alloy ($\sigma_Y$ = 117 MPa; $\sigma_{UTS}$ = 180 MPa; % EL = 14). Again, the strengths are higher than AA6061-O, but lower than AA6061-T4, and ductility is much lower than AA6061-O and AA6061-T4. The fracture surface on AC3 sample consisted of many cleavage facets as presented in Fig. 9(c) and (d) with the "river pattern," which indicates the low energy brittle fracture.

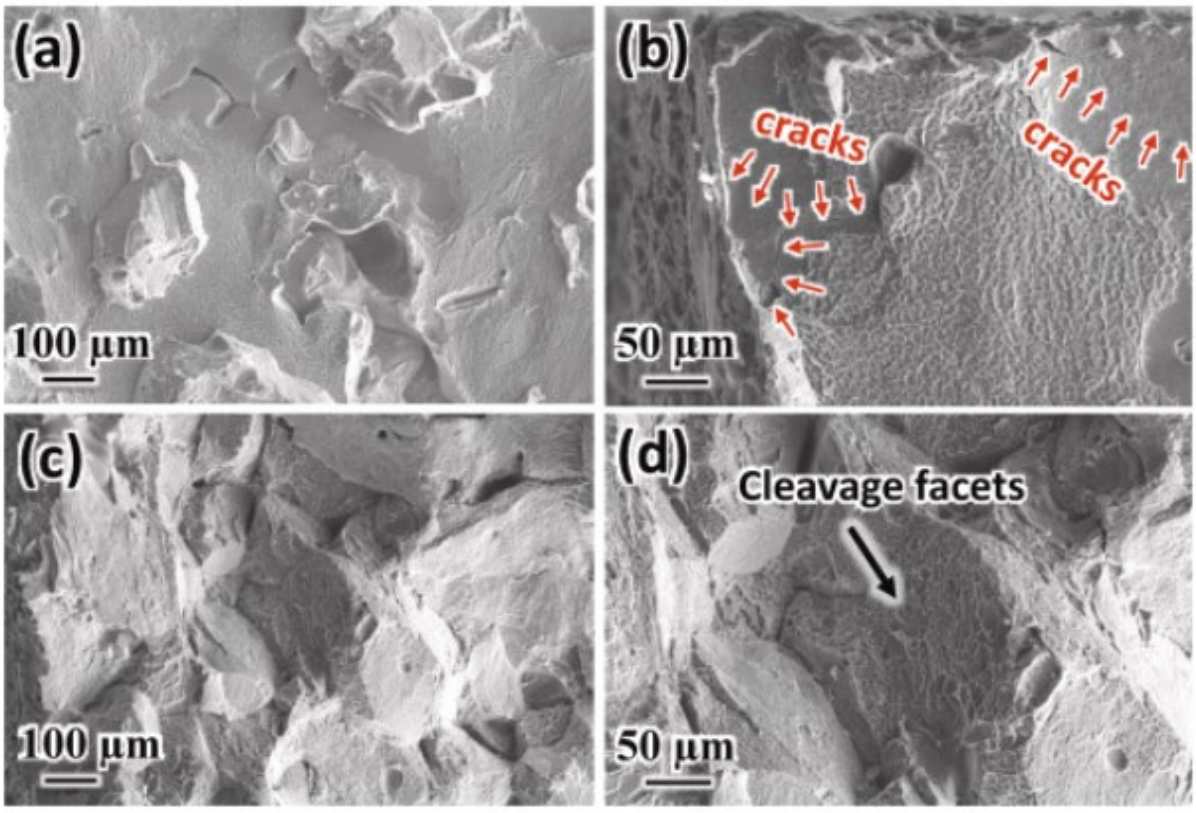


Fig. 9. Secondary electron micrograph from the fracture surface of the (a,b) AC2 and (c,d) AC3 tensile specimens.

Fracture path in FC2 ($\sigma_Y$ = 82 MPa; $\sigma_{UTS}$ = 131 MPa; % EL = 30) followed mostly in the bulk AA6061 alloy, not at the diffusion bonded interface, and these properties are equivalent to AA6061-O. Fig. 10(a) and (b) present the secondary electron micrographs and corresponding

backscatter electron micrographs (inset) of the fracture surfaces from FC2 samples. Many small dimples, corresponding to the ductile mode of fracture and elongation of 30 %, were observed. The fracture surface also shows the cracking within $Al_{19}Fe_4MnSi_2$ precipitates, and $Mg_2Si$ precipitates were observed at the bottom of the dimples. Fracture in FC3 occurred at the diffusion bonded interface at a similar strength to AA6061-O, but with a very low ductility ($\sigma_Y$ = 89 MPa; $\sigma_{UTS}$ = 120 MPa; % EL = 10). Fig. 10(c) and (d) present the secondary electron micrographs and corresponding backscatter electron micrographs (inset) of the fracture surface from FC3 samples. It consisted entirely of intergranular fracture which corresponds to the ductility lower than FC2. The fractured surface also depicts the presence of cracking within $Al_{19}Fe_4MnSi_2$ precipitates, and remnant $Mg_2Si$ precipitates (i.e. pull-out after fracture) observed at the bottom of the large pores in Fig. 10(d).

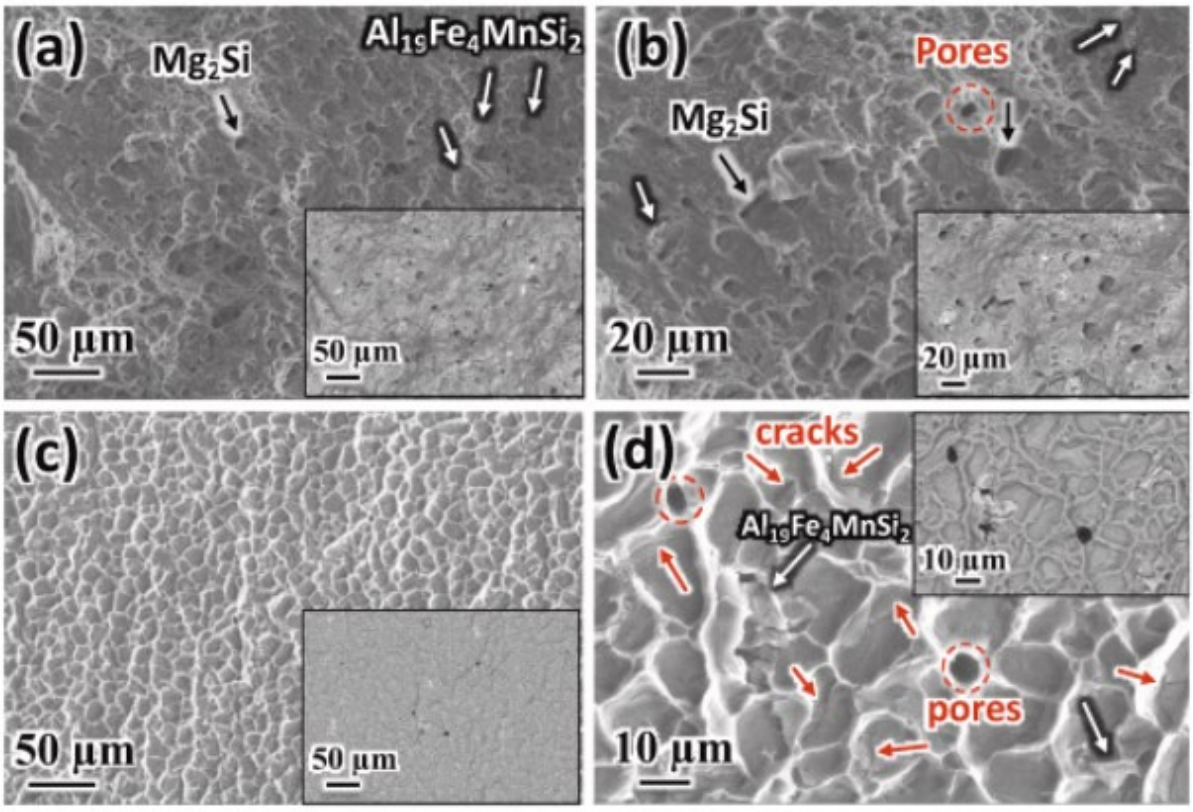


Fig. 10. Secondary electron micrograph and corresponding back scatter electron micrograph (inset) from the fracture surface of the (a, b) FC2 and (c, d) FC3 tensile specimens.

Fig. 11(a) presents the high magnification secondary electron micrograph from one of the cracks in the FC3 sample with the corresponding backscatter electron micrograph in Fig. 11(b). Fig. 11(c) presents XEDS spectrum from the overall fracture surface of AA6061 demonstrating the minor presence of Mg, Si, Cr, Fe, Cu, and Mn, consistent with the elemental composition of AA6061. Fig. 11(d) shows XEDS spectrum from the region indicated by the red arrow (one end of the crack) in Fig. 11(a) and (b). These results demonstrate a significant presence of Mg and Si, most likely due to a small amount of the left-over $Mg_2Si$, which would have been sheared and/or pulled-out

during tensile testing. Inset in Fig. 11(d) shows the low intensity peaks in the XEDS spectrum from $Mg_2Si$ precipitates depicting the absence of peaks from Cr, Fe, Cu, and Mn.

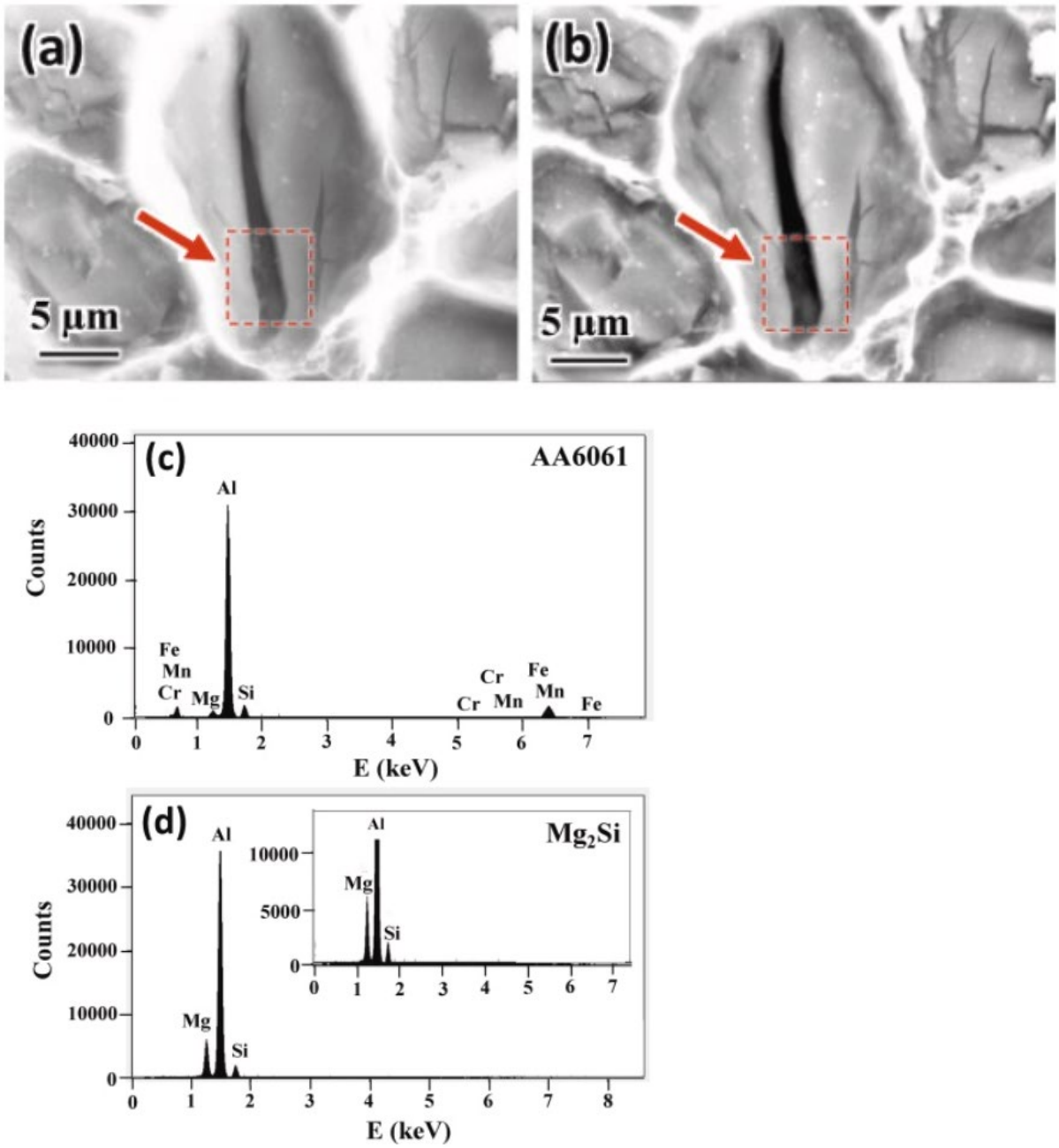


Fig. 11. (a) Secondary electron micrograph from a crack in FC3 sample and (b) corresponding backscatter electron micrograph. XEDS spectrum from the (c) bulk AA6061 alloy and (d) region indicated by the red arrow at the one end of the crack. Inset in (d) is a typical $Mg_2Si$ precipitates data collected from cross-sectional sample such as that shown in Fig. 2(c). (For interpretation of the references to colour in this figure legend, the reader is referred to the Web version of this article.)

Fig. 12(a) presents the secondary electron micrograph from the fracture surface depicting the presence of a pore and $Al_{19}Fe_4MnSi_2$ precipitates in the FC3 sample with the corresponding backscatter electron micrograph in Fig. 12(b). Fig. 12(c) shows XEDS spectrum from the $Al_{19}Fe_4MnSi_2$ precipitates with the elemental presence of Fe, Mn, Si, and Cr, without Mg. Fig. 12(d) shows XEDS spectrum from the region indicated by the red arrow in Fig. 12(a). Again, the presence of Mg and Si peaks suggests that the pore formed due to a possible pull out of $Mg_2Si$ during fracture. Quantification of phase constituents, e.g., matrix and precipitates, is challenging due to the fact that the z-contrast by backscatter electrons is difficult to distinguish between the $Mg_2Si$ and α-Al matrix, especially on the undulated fractured surfaces. Insets in Fig. 12(c) and (d) presents the low intensity peaks in XEDS spectrum from $Al_{19}Fe_4MnSi_2$ and $Mg_2Si$ precipitates.

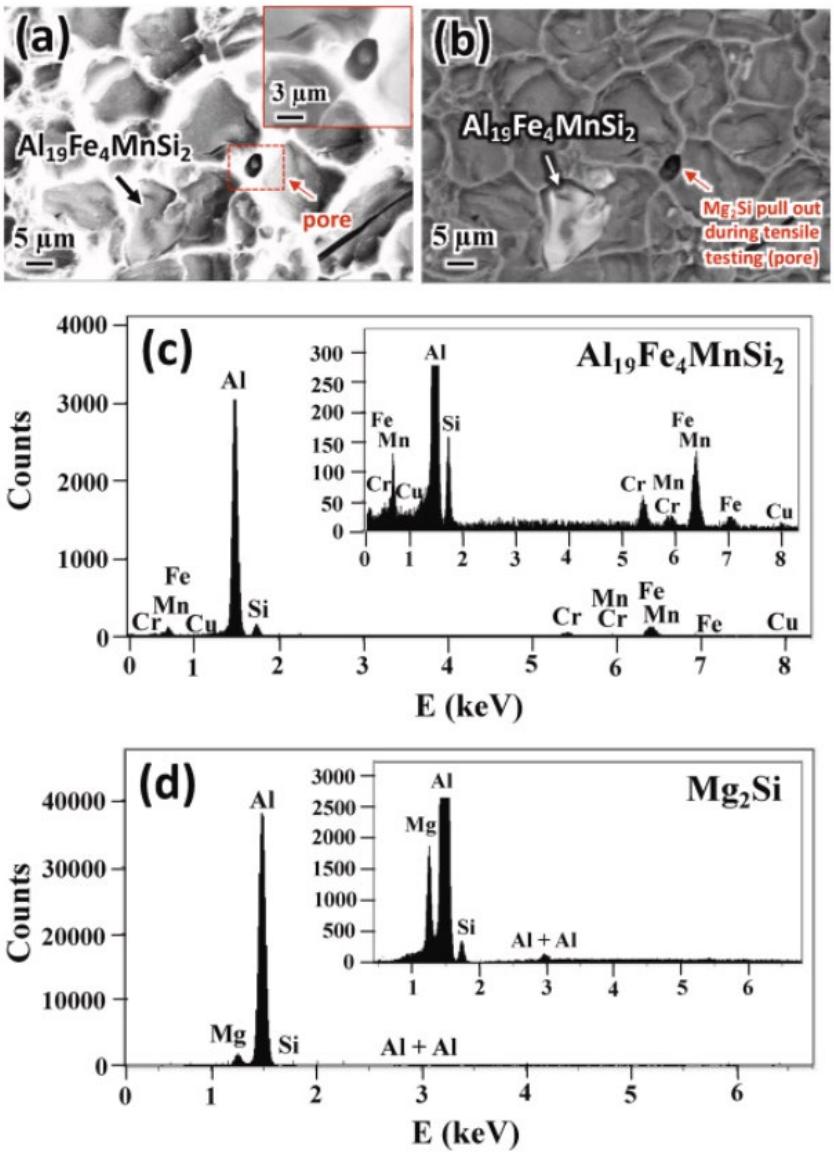


Fig. 12. (a) Secondary electron micrograph from a fracture surface depicting the presence of pore and $Al_{19}Fe_4MnSi_2$ precipitate in FC3 sample. (b) Corresponding back scatter electron micrograph of (a). XEDS energy spectra from the (c) $Al_{19}Fe_4MnSi_2$ precipitate and (d) region indicated by red

arrow in (a), depicting the possible pull out of $Mg_2Si$ during tensile testing. (For interpretation of the references to colour in this figure legend, the reader is referred to the Web version of this article.)

## 6. Modeling of mechanical behavior

To investigate the impact of concentrated $Mg_2Si$ precipitates at the diffusion bonded interface, a FEA was conducted by varying the linear density, i.e., the spacing between the precipitates, as listed in Table 2. Three different alloy properties were applied to AA6061 to analyze its tensile behavior at the diffusion bonded interface, corresponding to AA6061-O, -T4, and -T6 for furnace cooled, air cooled, and water quenched cooling methods, respectively. The simulation did not consider the effects of scale/surface phenomena. Therefore, the results were normalized to show a relative comparison of tensile properties on microstructural variation arising from the difference in post-anneal cooling rate. The $Al_{19}Fe_4MnSi_2$ precipitates that form during casting have a fixed number density, and their presence was incorporated into the matrix/bulk properties. Only a minor coarsening was observed experimentally, and its effect on the precipitate's number density with subsequent heat treatment was ignored.

Fig. 13(a) and (b) depict the von Mises equivalent stress distribution of AA6061-O at the interface and the corresponding equivalent plastic strain, respectively, from the FEA simulation when the engineering strain of the tensile bars is 0.1. In absence of $Mg_2Si$ precipitates, Von-Mises stresses are approximately 120∼140 MPa with negligible plastic strain. With the increase in precipitate linear density to 0.33, the Von-Mises stresses in the vicinity of the precipitates increases by ∼50% to 210 MPa, however the stress field between two adjacent precipitates largely remain unchanged. But when the linear density of $Mg_2Si$ precipitates increased to 0.5 the stress field interaction between adjacent precipitates increased from 140 to 190 MPa, and there is a three-fold or higher increase in the corresponding equivalent plastic strain. This clearly demonstrate the presence of significant stress concentration in the vicinity of the precipitates. With an increase in the linear density of precipitates, the area fraction with higher stress and plastic strain would also increase in the vicinity of the precipitates, causing failure at relatively low strain compared to other cases. The normalized elongation at failure (%EL) as a function of the linear density of $Mg_2Si$ precipitates is illustrated in Fig. 14(a). The %EL was normalized to that of the bulk alloy without any precipitate (i.e., $Mg_2Si$ linear density of 0) for each AA6061 type (i.e., AA6061-O, -T4, and -T6). The presence of concentrated precipitates at the interface considerably reduced the ductility (i.e., a reduction of nearly 70%) regardless of the AA6061 type.

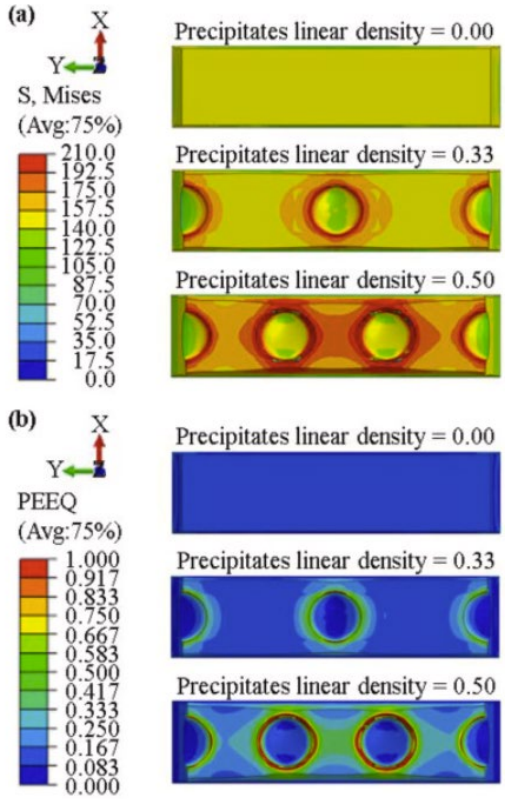


Fig. 13. (a) Von mises stress (b) equivalent plastic strain for O annealed AA6061 alloy from finite element analysis at engineering strain 0.1.

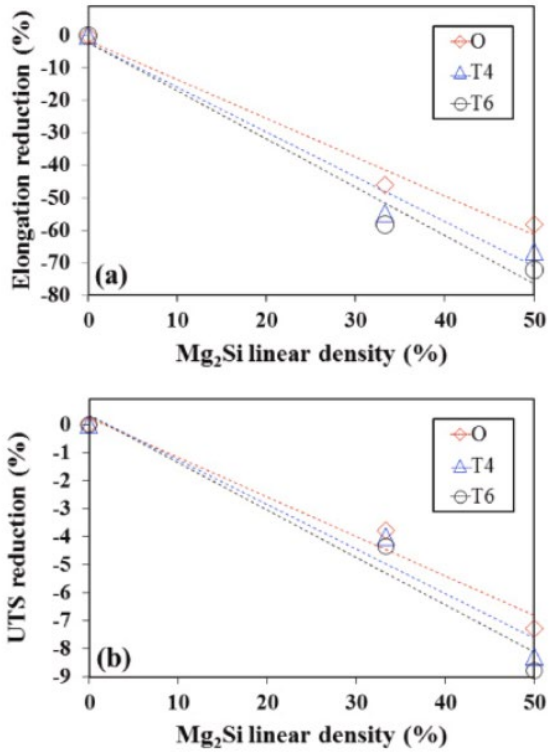

Fig. 14. (a) Normalized elongation at failure and (b) normalized UTS as functions of linear density of the $Mg_2Si$ precipitates.

Fig. 14(b) demonstrates that the variation in the linear density of $Mg_2Si$ precipitates had a minimal effect on the ultimate tensile strength (UTS) (i.e., a reduction of less than 10%). The change in UTS was predominantly caused by the variation in bulk alloy properties from the heat treatment (i.e., O, T4, or T6). Consequently, a furnace cooled diffusion couple with strengths comparable to AA6061-O, but with concentrated $Mg_2Si$ precipitates at the diffusion bonded interface, could potentially exhibit inconsistent and lower ductility (i.e., lower than AA6061-O), as observed experimentally. In contrast, the water quenched diffusion couple exhibited UTS and ductility similar to T6 (or T4) temper, without any concentrated $Mg_2Si$ precipitates at the diffusion bonded interface. These findings support the experimental results from the diffusion couples that exhibited lower and inconsistent %EL.

Fig. 7 presents a comparison between the experimental results and those obtained through FEA. In the FEA simulations, bulk alloy properties of AA6061-O, -T4, and -T6 were utilized for the diffusion couples that were furnace cooled, air cooled, and water quenched, respectively. The FEA was carried out for $Mg_2Si$ linear densities of 0, 33, and 50%, while the experimentally observed linear densities were 0, 17, and 46%. To estimate the yield strength, tensile strength, and elongation at failure for the experimentally observed linear densities, a linear interpolation was employed. For instance, the FEA results for the water-quenched diffusion couple shown in Fig. 7 were obtained using bulk properties of AA6061-T6 with 0 % $Mg_2Si$ precipitate linear density since no precipitates were observed. Conversely, the furnace cooled diffusion couple was simulated using bulk properties of AA6061-O with 46 % $Mg_2Si$ precipitate linear density in the FEA results. Despite the wide range of standard deviation in the elongation at break for the furnace cooled sample, the trends in mechanical behavior simulated by FEA were adequate in describing the experimental results.

## 7. Summary

This study investigated the tensile behavior of diffusion bonded AA6061 alloy with varying cooling methods to mimic the thermal history of HIP bonded AA6061 cladding during fabrication of monolithic fuel plates. The diffusion bonding process consisted of isothermal anneal at 560 °C for 1.5 h. Three different cooling methods were employed, namely furnace cooling, air cooling, and water quenching. Furnace cooled specimens with extensive $Mg_2Si$ precipitates at the bond interface exhibited yield and tensile strengths similar to AA6061-O but with reduced/inconsistent ductility. Water quenched specimens without any formation of $Mg_2Si$ precipitates at the interface exhibited yield and tensile strengths similar to AA6061-T4 and ductility similar to AA6061-T6. Finite element analysis demonstrated that these trends are strongly influenced by both the matrix/bulk alloy properties and the concentrated presence of $Mg_2Si$ at the interface. Overall, the study shows that the strength is dominated by the matrix/bulk properties of AA6061, while ductility is strongly influenced by the presence of $Mg_2Si$ precipitates at the diffusion bonded interface. The microstructural development and the corresponding mechanical behavior at the AA6061 HIP interface would be essential to understand the performance of the monolithic fuel system produced by HIP.

## CRediT authorship contribution statement

**Abhishek Mehta:** Conceptualization, Methodology, Validation, Formal analysis, Investigation, Data curation, Writing – original draft, Visualization. **Jeongmin Woo:** Validation, Investigation, Data curation, Writing – original draft, Visualization. **Jeffrey J. Giglio:** Conceptualization, Formal analysis, Resources, Supervision, Project administration, Funding acquisition. **Jan-Fong Jue:** Conceptualization, Formal analysis, Resources, Supervision, Project administration, Funding acquisition. **Dennis D. Keiser:** Conceptualization, Resources, Data curation, Supervision, Project administration, Funding acquisition. **James I. Cole:** Conceptualization, Resources, Data curation, Supervision, Project administration, Funding acquisition. **Yongho Sohn:** Conceptualization, Methodology, Resources, Writing – review & editing, Visualization, Supervision, Project administration, Funding acquisition.

## Declaration of competing interest

The authors declare the following financial interests/personal relationships which may be considered as potential competing interests:Yongho Sohn reports financial support was provided by U.S. Department of Energy, Office of Nuclear Materials Threat Reduction (NA-212), National Nuclear Security Administration, under DOE-NE Idaho Operations Office Contract DE-AC07-05ID14517.

## Acknowledgements

This work was supported by the U.S. Department of Energy, Office of Nuclear Materials Threat Reduction (NA-212), National Nuclear Security Administration, under DOE-NE Idaho Operations Office Contract DE-AC07-05ID14517. Accordingly, the U.S. Government retains a non-exclusive, royalty-free license to publish or reproduce the published form of this contribution, or allow others to do so, for U.S. Government purposes.

References

[1]D.D. Keiser, S.L. Hayes, M.K. Meyer, C.R. Clark, High-density, low-enriched uranium fuel for nuclear research reactors, J. Occup. Med. 55 (9) (2003) 55–58.

[2]J.L. Snelgrove, G.L. Hofman, M.K. Meyer, C.L. Trybus, T.C. Wiencek, Development of very-high-density low-enriched-uranium fuels, Nucl. Eng. Des. 178 (1) (1997) 119–126.

[3]A.L.S. van den Berghe, E. Koonen, L. Sannen, From high to low enriched uranium fuel in research reactors, Adv. Sci. Technol. 73 (2010) 78–90.

[4]A. Mehta, J. Dickson, R. Newell, D.D. Keiser, Y. Sohn, Interdiffusion and reaction between Al and Zr in the temperature range of 425 to 475 C, J. Phase Equilibria Diffus. 40 (4) (2019) 482–494.

[5]A. Mehta, N. Eriksson, R. Newell, L. Zhou, E. Schulz, W. Sprowes, F. Betancor, Y. Park, D.D. Keiser, Y. Sohn, Phase transformations and microstructural development in the U-10 Wt pct Mo

alloy with varying Zr contents after heat treatments relevant to the monolithic fuel plate fabrication process, Metall. Mater. Trans. 50 (1) (2019) 72–96.

[6]R. Newell, A. Mehta, Y.J. Park, Y.H. Sohn, J.F. Jue, D.D. Keiser Jr., Relating diffusion couple experiment results to observed as-fabricated microstructures in low-enriched U-10wt.% Mo monolithic fuel plates, Defect Diffusion Forum 375 (2017) 18–28.

[7]R. Newell, A. Mehta, Y.J. Park, D.D. Keiser Jr., Y.H. Sohn, Interdiffusion, reactions, and phase transformations observed during fabrication of low enriched uranium monolithic fuel system for research and test reactors, Defect Diffusion Forum 383 (2018) 10–16.

[8]R. Newell, A. Mehta, Y. Park, D. Keiser Jr., J. Cole, Y. Sohn, Microstructural characteristics of plasma sprayed, electroplated, and co-rolled Zr diffusion barriers in hot isostatic pressed low enriched U-10 wt% Mo monolithic fuel plates, J. Nucl. Mater. 523 (2019) 91–100.

[9]R. Newell, Y. Park, A. Mehta, D. Keiser, Y. Sohn, Mechanical properties examined by nanoindentation for selected phases relevant to the development of monolithic uranium-molybdenum metallic fuels, J. Nucl. Mater. 487 (2017) 443–452.

[10]J.-F. Jue, D.D. Keiser, C.R. Breckenridge, G.A. Moore, M.K. Meyer, Microstructural characteristics of HIP-bonded monolithic nuclear fuels with a diffusion barrier, J. Nucl. Mater. 448 (1) (2014) 250–258.

[11]Y. Park, R. Newell, A. Mehta, D. Keiser Jr., Y. Sohn, Interdiffusion and reaction between U and Zr, J. Nucl. Mater. 502 (2018) 42–50.

[12]E.A. Schulz, A. Mehta, I.V. Belova, G.E. Murch, Y. Sohn, Simultaneous measurement of isotope-free tracer diffusion coefficients and interdiffusion coefficients in the Cu-Ni system, J. Phase Equilibria Diffus. 39 (6) (2018) 862–869.

[13]E. Schulz, A. Mehta, S.H. Park, Y. Sohn, Effects of marker size and distribution on the development of kirkendall voids, and coefficients of interdiffusion and intrinsic diffusion, J. Phase Equilibria Diffus. 40 (2019) 156–169.

[14]A. Mehta, L. Zhou, D.D. Keiser Jr., Y. Sohn, Anomalous growth of Al8Mo3 phase during interdiffusion and reaction between Al and Mo, J. Nucl. Mater. 539 (2020), 152337.

[15]L. Zhou, A. Mehta, K. Cho, Y. Sohn, Composition-dependent interdiffusion coefficient, reduced elastic modulus and hardness in γ-, γ′-and β-phases in the Ni-Al system, J. Alloys Compd. 727 (2017) 153–162.

[16]A. Mehta, Y. Sohn, Interdiffusion, solubility limit, and role of entropy in FCC Al-Co- Cr-Fe-Ni alloys, Metall. Mater. Trans. 51 (6) (2020) 3142–3153.

[17]A. Mehta, Y. Sohn, High entropy and sluggish diffusion “core” effects in senary FCC Al–Co–Cr–Fe–Ni–Mn alloys, ACS Comb. Sci. 22 (12) (2020) 757–767.

[18]A. Mehta, I.V. Belova, G.E. Murch, Y. Sohn, Measurement of interdiffusion and tracer diffusion coefficients in FCC Co-Cr-Fe-Ni multi-principal element alloy, J. Phase Equilibria Diffus. 42 (2021) 696–707.

[19]R.H.S. Winterton, Newton's law of cooling, Contemp. Phys. 40 (3) (1999) 205–212.

[20]B.C. Salzbrenner, J.M. Rodelas, J.D. Madison, B.H. Jared, L.P. Swiler, Y.-L. Shen, B. L. Boyce, High-throughput stochastic tensile performance of additively manufactured stainless steel, J. Mater. Process. Technol. 241 (2017) 1–12.

[21]A. Mehta, L. Zhou, E.A. Schulz, D.D. Keiser, J.I. Cole, Y. Sohn, Microstructural characterization of AA6061 versus AA6061 HIP bonded cladding–cladding interface, J. Phase Equilibria Diffus. 39 (2) (2018) 246–254.

[22]ASM Metals Handbook: Volume 2: Properties and Selection: Non Ferrous Alloys and Special-Purpose Materials, ASM International, Ohio, 1992.

[23]E.F.A. Zeid, Mechanical and electrochemical characteristics of solutionized AA 6061, AA6013 and AA 5086 aluminum alloys, J. Mater. Res. Technol. 8 (2) (2019) 1870–1877.

[24]A. Kacem, A. Krichen, P.Y. Manach, S. Thuillier, J.W. Yoon, Failure prediction in the hole-flanging process of aluminium alloys, Eng. Fract. Mech. 99 (2013) 251–265.

[25]H. Talebi Ghadikolaee, H. Moslemi Naeini, M.J. Mirnia, M.A. Mirzai, S. Alexandrov, H. Gorji, Experimental and numerical investigation of failure during bending of AA6061 aluminum alloy sheet using the modified Mohr-Coulomb fracture criterion, Int. J. Adv. Des. Manuf. Technol. 105 (2019) 5217–5237.

[26]A. Li, X.P. Zhao, H.Y. Huang, Y. Ma, L. Gao, Y.J. Su, P. Qian, Fine-tuning the ductile-brittle transition temperature of $Mg_2Si$ intermetallic compound via Al doping, Int. J. Miner. Metall. Mater. 26 (2019) 507–515.

[27]H. Ozaltun, P.G. Medvedev, Structural Behaviour of Monolithic Fuel Plates during Hot Isostatic Pressing and Annealing, US DOE Report (Idaho National Laboratory), 2010. INL/CON-09-17428.

[28]W. Soboyejo, Mechanical Properties of Engineered Materials, CRC press, 2002.

[29]R.D. Schmidt, E.D. Case, J. Giles, J.E. Ni, T.P. Hogan, Room-temperature mechanical properties and slow crack growth behavior of $Mg_2Si$ thermoelectric materials, J. Electron. Mater. 41 (6) (2012) 1210–1216.

[30]Y. Bao, T. Wierzbicki, On fracture locus in the equivalent strain and stress triaxiality space, Int. J. Mech. Sci. 46 (1) (2004) 81–98.

[31]Y. Bai, X. Teng, T. Wierzbicki, On the Application of Stress Triaxiality Formula for Plane Strain Fracture Testing, 2009.

[32]W. Kolmogorov, Spannungen deformationen bruch, Metallurg 230 (1970).

[33]A.N. Abood, A.H. Saleh, Z.W. Abdullah, Effect of heat treatment on strain life of aluminum alloy AA 6061, J. Mater. Sci. Res. 2 (2) (2013) 51.

[34]G. Modlen, Manufacturing engineering and technology. By serope kalpakjian (Addison-Wesley, 1989.), Int. J. Prod. Res. 28 (2) (1990), 431-431.

[35]M.N. Amado, F. Daroqui, Revision of the solvus limit of Al-$Mg_2Si$ pseudo binary phase diagram, Procedia Materials Science 8 (2015) 1079–1088.

[36]R.R. Ambriz, G. Barrera, R. García, V.H. L´opez, Effect of the weld thermal cycles of the modified indirect electric arc on the mechanical properties of the AA6061-T6 alloy, Weld. Int. 24 (4) (2010) 321–328.

[37]T. Ajantiwalay, H. Vo, R. Finkelstein, P. Hosemann, A. Aitkaliyeva, Towards bridging the experimental length-scale gap for tensile tests on structural materials: lessons learned from an initial assessment of microtensile tests and the path forward, Jom 72 (2020) 113–122.